Highly depth-resolved chirped pulse photothermal radar for bone diagnostics

Sreekumar Kaiplavil and Andreas Mandelis
Center for Advanced Diffusion-Wave Technologies, Department of Mechanical and Industrial Engineering, University of Toronto, 5 King's College Road, Toronto, Ontario M5S 3G8, Canada

(Received 16 May 2011; accepted 5 July 2011; published online 28 July 2011)

A novel chirped pulse photothermal (PT) radiometric radar with improved sensitivity over the conventional harmonically modulated thermal-wave radar technique and alternative pulsed laser photothermal radiometry is introduced for the diagnosis of biological samples, especially bones with tissue and skin overlayers. The constraints imposed by the laser safety (maximum permissible exposure) ceiling on pump laser energy and the strong attenuation of thermal-wave signals in tissues significantly limit the photothermally active depth in most biological specimens to a level which is normally insufficient for practical applications (a few mm below the skin surface). A theoretical approach for improvement of signal-to-noise ratio (SNR), minimizing the static (dc) component of the photothermal signal and making use of the photothermal radiometric nonlinearity has been introduced and verified by comparing the SNR of four distinct excitation wave forms (sine-wave, square-wave, constant-width and constant duty-cycle pulses) for chirping the pump laser, under constant exposure energy. At low frequencies fixed-pulsewidth chirps of large peak power were found to be superior to all other equal-energy modalities, with an SNR improvement up to two orders of magnitude. Distinct thickness-dependent characteristic delay times in a goat bone were obtained, establishing an active depth resolution range of ~2.8 mm in a layered skin-fat-bone structure, a favorable result compared to the maximum reported pulsed photothermal radiometric depth resolution <1 mm in turbid biological media. © *2011 American Institute of Physics*. [doi:10.1063/1.3616140]

I. INTRODUCTION

Photothermal (PT) science has made remarkable achievements in the development of measurement schemes of importance in basic science, engineering and medical technology during the past four decades.[1–3] PT techniques, which make use of the principles of diffusion-wave phenomena, basically examine the resulting thermal or acoustic waves, photoexcited charge carriers, phonons and absorbed or scattered photons in a medium following periodic optical excitation. The successful applications of diffusion-wave science extend over a wide spectrum that covers measurement of thermophysical parameters of solids and fluids,[4–7] microscopy and tomography,[8–10] wide field imaging and thermography,[11,12] non-invasive dental diagnostics,[13] microelectronic metrology,[14] etc. In medicine and biology, both time- and frequency-domain PT analytical methods have been successful for non-invasive measurements of peripheral and subsurface tissue parameters.[15–17] Imaging of deep lying dental carries has been accomplished with better sensitivity than x-rays (radiographs), with frame synchronized PT wave detection ("dental thermophotonic imaging").[18] PT imaging of tumors and infections with the aid of nano-particle contrast agents,[19] single bio-molecule identification[20] and nanocluster assisted cellular imaging[21] are a few among the recent promising applications of PT research in the biomedical field.

The PT radar is a modality that benefits from an improved depth profiling capability compared to conventional PT techniques. This technique is of importance if the specimen of interest contains multiple sources of thermal waves lying at different depths. If these sources have the same lateral coordinates and only differ in the depth (z) coordinate, it is difficult to identify (resolve) them using conventional photothermal frequency-scan techniques with a harmonic thermal wave diffusing along the z direction. This is so because single-frequency thermal waves yield depth-integrated information from approximately one thermal diffusion length. In contrast, the photothermal radar yields depth resolved information and thus is ideally suited for probing subsurface interfaces such as bone surfaces with tissue and skin overlayers. Our laboratory[22–24] and other groups[25] have introduced photothermal cross-correlation (pulse compression) radar techniques in which the laser modulation is frequency chirped. A chirp signal with start and end frequencies f_S and f_E, respectively, and repetition time T is used to modulate the pump laser beam. The resulting thermal waves from the sample are also chirped, yet embedded in noise. Pulse compression is performed by computing the cross correlation between a reference chirp and the resulting photothermal signal chirp. Several biological sources (skin, fat, tissues, blood, bone, etc.), which are at different depths, contribute to the resulting signal at the skin surface. The latter is detected non-invasively by an infrared detector in the case of infrared photothermal radiometry (PTR). If $R(\tau)$ and $S(t+\tau)$ are the reference waveform and the responsive signal, respectively, the latter being measured at the delay time t, then the cross correlation is defined by

$$C_R(t) = \int_{-\infty}^{\infty} R^*(\tau) S(t+\tau) d\tau. \quad (1)$$

Here, $R^*(\tau)$ is the complex conjugate of the reference signal. In the case of multiple sources, at different depths, the conductive component of the PTR signal takes longer than the radiative (emissive) component to reach the surface. When the resulting composite signal is pulse compressed using correlation with the reference chirp, the output will contain a delayed peak, the delay being a function of the thermophysical properties and the depth of sources below the plane of detection.

While extending the applicability of PT techniques to biological tissues, the major factor of concern is the ability to resolve deep lying absorbers. Reports using pulsed photothermal radiometry (PPTR) have shown that subsurface absorber detection limits in turbid media and tissue are ~1 mm.[26,27] However, any successful development of photothermal diagnostic technologies for bone characterization necessitates capturing thermal waves generated over a depth of a few mm below the skin surface in the soft-hard tissue matrix. Furthermore, laser-induced photothermal signal quality (SNR) is limited by the ceiling of the safety standard curve for maximum permissible exposure (MPE) with regard to laser power excitation of human tissues.[28] Therefore, any further improvement in PTR depth resolution will have to be associated with substantial SNR enhancement. Relatively low optical absorption in the therapeutic optical window (700–1300 nm) and strong absorption of infrared (IR) photons by water molecules in tissues make the available depth information carried by the conventional PTR signal at the skin surface too limited for biologically reliable diagnosis. Consequently, development of PT technologies of practical importance for medical applications is very challenging. In this paper, we describe the development of a depth-resolution optimized PTR radar-based technique for the characterization of human bones aimed at establishing a technology for the early diagnosis of osteoporosis. Tissue and skin overlayers strongly attenuate photothermal waves generated in a bone and hence conductive thermal coupling between the bone and skin surface (plane of detection) becomes weak. In addition, strong re-absorption of emitted IR photons by water molecules in overlying tissue may forbid radiative coupling. In view of the fact that for realistic applications through the skin surface generated by subsurface bones, PTR signals demand superior instrumental SNR, in this report, we introduce a new chirped pulse photothermal radar and its PTR implementation. The new method exhibits much improved SNR and depth profiling capabilities superior to pulsed PTR (Refs. 26 and 27) and to the conventional harmonically modulated PTR radar[22,25] for the same optical energy exposure.

II. THEORY OF OPTIMUM PHOTOTHERMAL RADAR SNR

A. Surface thermal-wave field

The PT signal response of a black absorber in the frequency domain is considered for one-dimensional (1D) and three-dimensional (3D) thermal waves produced under sine-wave (harmonic) excitation. Under chirp excitation both the PT signal (ac) and static temperature rise (dc background) components must be examined, the latter being cumulative in nature over several chirp repetition cycles. In agreement with conservation of energy, a method that minimizes the static component would result in stronger ac component under similar boundary convection and/or radiation heat loss conditions (or if boundary losses are negligible). The optimization problem is the identification of suitable excitation waveforms to meet this ac signal maximization requirement for PTR (and other PT techniques). As long as no phase transitions occur, or radiative energy transfer or photochemical reactions, the energy absorbed by a sample following modulated laser beam excitation will appear both as *ac* PT signal and static temperature rise. A fraction of the converted optical-to-thermal energy will also be lost to convection and/or radiation at interfaces. Since the major objective of this work is to maximize the *ac* PT signal, the relative ac and dc component magnitudes will be examined as a function of the diffusion length and laser spot size, i.e., the key spatial parameters controlling thermal-wave transport. We consider a semi-infinite isotropic sample irradiated with a Gaussian laser beam of spot size radius a at $1/e^2$ of the peak intensity and peak power P, modulated sinusoidally with an angular frequency ω. Assuming perfect optical absorption at the surface (unity non-radiative energy conversion coefficient), if the spot size is smaller than the thermal diffusion length the three-dimensional thermal-wave regime will ensue with the cylindrical symmetry of the laser beam. The resulting temperature distribution on the surface can be expressed as

$$T(\vec{r}, t; \omega) = T_0 + T_{dc}(\vec{r}, t; \omega) + T_{ac}(\vec{r}, t; \omega). \tag{2}$$

Here, $\vec{r}$ is the radial coordinate, T_0 is the ambient temperature, T_{dc} is the dc component of the thermal field, and T_{ac} is the PT signal. The fact that most experimental configurations are not ideally adiabatic in nature makes the last two terms strongly dependent on the dynamics of heat loss via convection and/or radiation. This renders the static temperature field a frequency-dependent parameter.[29,30] The dependence of T_{dc} and T_{ac} on modulation frequency must be considered separately for identifying the optimum conditions for signal enhancement.

If k denotes the thermal conductivity of the probed material, a Hankel-space description of the 3D ac photothermal response can be described as[31,32]

$$T_{ac}(r, z) = \frac{Pa^2}{k} \int_0^\infty \frac{1}{\beta} e^{-\beta z - (\lambda^2 a^2/4)} J_0(\lambda r) \lambda d\lambda, \tag{3}$$

where a is the laser beam spotsize, $\beta(\omega) = \sqrt{\lambda^2 + \sigma(\omega)^2}$ and $\sigma(\omega)$ is the complex thermal wavenumber: $\sigma(\omega) = \sqrt{i\omega/\alpha}$. Here α is the thermal diffusivity of the material. J_0 is the Bessel function of the first kind and zeroth order, λ is the Hankel variable, and r and z denote radial and axial heat flow, respectively. If all boundary losses are neglected (adiabatic limit), the PT signal at the surface and at the center of the beam axis is given by

$$T_{ac}(r = 0, z = 0) = \frac{Pa^2}{k} \int_0^\infty \frac{1}{\beta} e^{-(\lambda^2 a^2/4)} \lambda d\lambda. \tag{4}$$

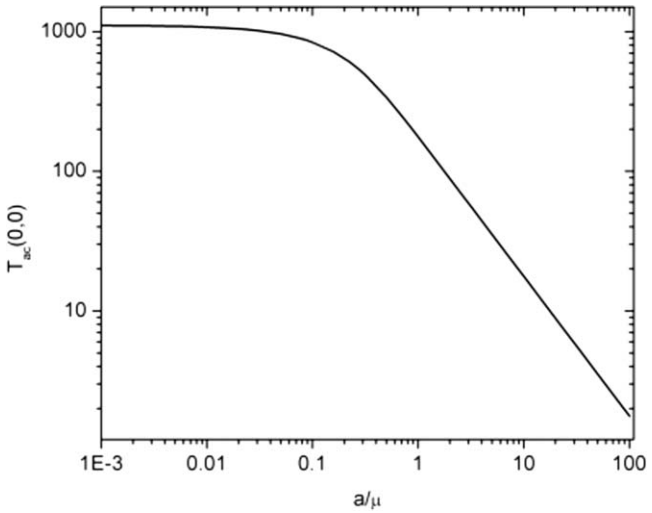

FIG. 1. Simulated amplitude of thermal wave signal at the surface of an optically opaque and thermally thick sample spanning the ranges of one-dimensional ($a/\mu > 1$) and three-dimensional ($a/\mu < 1$) thermal-wave diffusion.

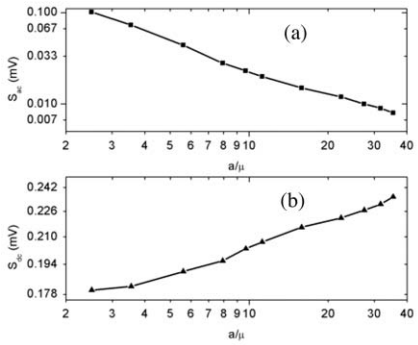

FIG. 2. Complementary behavior of ac (a) and dc (b) PTR signal components as a function of a/μ, for one-dimensional thermal-wave diffusion in glassy carbon.

In Fig. 1, $T_{ac}(r = 0, z = 0)$ is plotted against the ratio a/μ, spanning both three-dimensional ($a/\mu < 1$) and one-dimensional ($a/\mu > 1$) photothermal-wave regimes, with $\mu(\omega) = \sqrt{k/\pi f \rho c}$ being the thermal diffusion length. Here, f is the modulation frequency and ρ and c are the density and specific heat of the material, respectively. It is clear that the one-dimensional regime is attained at large beam diameter-to-diffusion-length values which is also the case of the experiments performed in this work. For the development of the optimum SNR photothermal radar technique, vitreous (glassy) carbon has been selected as the preferred test sample, as it has well-known thermophysical properties, produces strong photothermal signals and is fully optically opaque, with $k = 3.2$ W m^{-1} K^{-1}, $\rho = 1400$ kg m^{-3} and $c = 720$ J kg^{-1} K^{-1}.[33] The laser beam spot size radius a used for plotting Fig. 1 was 100 μm.

B. Photothermal radar signal-to-noise ratio enhancement

In most cases, thermal diffusion in biological tissues is one-dimensional due to their extreme light scattering nature. Therefore, we confine the current discussion to one-dimensional thermal diffusion for which there is a ω^{-1} dependence for the *ac* component in the thermally thick, 1D limit, as shown in Fig. 1. The experimentally measured *ac* and *dc* components for a thermally thick glassy carbon disc (4 cm in diameter and 1-cm thick) are plotted against a/μ in Fig. 2. Here $a = 0.5$ cm and the peak power is 500 mW. Using sinusoidal excitation and a conventional PTR set-up,[34] the signal was measured as a function of frequency and was recorded with a storage oscilloscope. In these measurements, the peak laser power remained fixed. Therefore, the energy delivered to the sample over a time interval large compared to the chirp repetition period was practically independent of modulation frequency. So, a flat *dc* response in the a/μ plot is expected, which is true for a lossless (adiabatic) experimental arrangement. Nevertheless, the *dc* component is found to increase with a/μ, the cause of which can be attributed to boundary heat losses for long excitation periods. The characteristic times for building up convective effects for various sample/heating configurations are well documented in the literature:[29,30] The convective loss factor is high if the modulation period is longer than the time for establishing free convection for a sample/experimental configuration which is not perfectly adiabatic. As frequency increases, the loss factor decreases, leading to a progressive build-up in the static component of the thermal field. The expected complementary nature of *ac* and *dc* signals in the frequency domain is demonstrated in Fig. 2 which implies that the use of low frequencies would be an effective means to minimize the *dc* component so that the *ac* signal will be enhanced. Low frequencies are also consistent with maximizing thermal-wave depth penetration. A reasonable optical waveform choice to achieve this is a pulse train with low duty cycle that gives the sample sufficient time to cool down to a temperature as close to the background as possible between successive pulses. If the pulse repetition period is longer than the boundary surface characteristic loss time, then the *dc* component or the baseline is greatly reduced thereby enhancing the modulated signal. Furthermore, since the pulse duration is short, large peak powers can be applied while maintaining low exposure energies within the MPE limits. This concept forms the second major criterion for signal enhancement. In PTR this can be further quantified using Stefan's law, according to which the net energy exchange per unit time and area of a radiator (sample surface) at temperature T, with its surroundings (IR detector) at temperature T_0 (assumed to be the room temperature), is

$$E = \varepsilon \sigma_{SB} \left(T^4 - T_0^4\right) \quad [\mathrm{Wm^{-2}K^{-4}}]. \tag{5}$$

Here, ε is the emissivity of the sample surface and σ_{SB} is the Stefan-Boltzmann constant. If the change in temperature of the sample with respect to room temperature T_0 is ξ, then

$$E = \varepsilon \sigma_{SB} \left((T_0 + \xi)^4 - T_0^4\right), \tag{6}$$

or, expanding

$$E = 4\varepsilon\sigma_{SB}T_0^3\xi\left(1+\frac{3}{2}\left(\frac{\xi}{T_0}\right)+\left(\frac{\xi}{T_0}\right)^2+\frac{1}{4}\left(\frac{\xi}{T_0}\right)^3\right). \tag{7}$$

It is evident from Eq. (7) that the detected PTR signal is linear with temperature only for very small temperature changes in the irradiated sample. It is also clear that nonlinearity will boost the PTR signal. Short optical pulses of high peak power generate thermal transients of large amplitudes and the resulting PT nonlinearity should improve SNR at the cost of increased interpretation complexity. In conclusion, a PTR radar excitation scheme that minimizes the static temperature component while introducing some nonlinearity would be beneficial for SNR enhancement (see Sec. III). Although the quantitative physical interpretation of the cross-correlation signals becomes complicated, the enhanced SNR of the nonlinear response adds sensitivity to the signal dependence on sample optical and thermophysical properties.

C. Chirp energy calculation and SNR estimation

The SNR optimization rationale developed so far points toward fixed-width or low-duty-cycle pulse chirps as potential candidates for optical excitation in the PTR radar modality for highly depth-resolved biomedical applications. To validate this, the SNR for a few common waveforms was experimentally compared in such a way that the chirp energy, the starting and ending frequencies, f_S and f_E, respectively, as well as chirp duration, T, were the same for all waveforms over one chirp repetition period. The total energy criterion used was that of compliance with the MPE curve. Linear frequency modulated (LFM) chirps of sine wave, square wave, pulse train of fixed pulsewidth, and pulse train of fixed duty cycle were considered for optical excitation. The first phase of SNR comparison was the evaluation of chirp energy over a chirp period for the various waveforms in terms of the signal parameters. Once this was done, energy equalization was accomplished by adjusting parameters like optical power, pulse width, duty cycle, etc. In this section, chirp energies are for the waveforms of interest.

For a sine wave, the LFM chirp with peak power $P = 2b$ (b: waveform amplitude), contains energy

$$E_{\sin} = b\int_0^T \{1+\sin[2\pi(f_S+Kt^2)]\}dt. \tag{8}$$

Here,

$$K = \frac{f_E - f_S}{T}. \tag{9}$$

Equation (8) is defined in terms of the Fresnel sine and cosine integrals $S(x)$ and $C(x)$, respectively:

$$E_{\sin} = bT + \frac{b}{\sqrt{K}}\sqrt{\frac{\pi}{2}}\begin{pmatrix}\cos\left[\frac{f_S^2}{4K}\right]\left(-S\left[\frac{f_S}{\sqrt{K}\sqrt{2\pi}}\right]+S\left[\frac{f_S+2KT}{\sqrt{K}\sqrt{2\pi}}\right]\right)+\\ \left(C\left[\frac{f_S}{\sqrt{K}\sqrt{2\pi}}\right]-C\left[\frac{f_S+2KT}{\sqrt{K}\sqrt{2\pi}}\right]\right)\sin\left[\frac{f_S^2}{4K}\right]\end{pmatrix}, \tag{10}$$

where, $S(x) = \int_0^x \sin(t^2)dt$ and $C(x) = \int_0^x \cos(t^2)dt$ which can be evaluated numerically. A square wave and a sine wave have equal energy if their peak powers are equal. Therefore, a square wave chirp of peak power $P = 2b$ has the same energy as the sine chirp above. Since the duty cycle of a square wave is 50%, the energy of a pulse chirp of duty cycle d% can be calculated to be $(d/50)E_{sq}$, where E_{sq} is the energy of a square wave chirp of equal peak power. For a pulse chirp of fixed width δ and peak power P, the energy is

$$E_{\text{fixed-width}} = P\delta N, \tag{11a}$$

where N is the number of pulses within one chirp period. Over the full chirp period T we obtain

$$E_{\text{fixed-width}} = P\delta\int_0^T (f_S+Kt)\,dt = P\delta T\left(\frac{f_S+f_E}{2}\right). \tag{11b}$$

The SNRs for these waveforms are experimentally determined in Sec. III. The chirp energy was equalized by suitably adjusting the wave parameters in Eqs. (10)–(11b) for the same frequency bandwidth and chirp duration.

Various noise sources associated with the excitation and detection instrumentation and the nature of their dependence on the pump laser modulation waveform parameters must be considered. A major question is whether there exists a correlation between noise power and chirp energy. In most of our applications, the detection bandwidth was less than 10 kHz with *dc* coupling for signal acquisition. The noise generated by the IR detector and signal processing instruments contains mainly Schottky, Johnson and 1/*f* components. For the pump laser, intensity fluctuation is the major noise source. None of these types of noise varies with laser power or pulse duration and the noise floor remains unaltered as long as the frequency bandwidth is fixed. This fact is important as it simplifies the SNR determination in the comparative waveform analysis, because one does not have to quantify the individual noise components. The overall noise power controls the measurement uncertainty not only of the PT radar peak height but also of the peak delay time. Since our parameter of interest is

the peak delay time for all waveforms, the SNR is calculated in terms of the mean value of delay (mean) and the standard deviation (SD), for all data sets using the relation:

$$\text{SNR} = \frac{\text{Mean}}{\text{SD}}. \tag{12}$$

For a sample with given optical, thermophysical and geometric properties, the cross-correlation peak delay time is fixed and is independent of laser power. Therefore, higher SNR indicates lower standard deviation, which translates into lower uncertainty in the peak delay time measurement and ultimately higher absorber sensitivity and depth resolution of the chirped PTR signal response.

III. EXPERIMENTAL AND RESULTS

For the four distinct PTR radar excitation waveforms under consideration some minor adjustments in the instrumental arrangement are necessary, especially in the signal generation system and laser source. Nevertheless, the general experimental arrangement remains the same. Figure 3 shows the block schematic of the instrumentation that can perform pulsed and fixed duty-cycle modulation. A signal generator (Agilent 33220 A) generates the chirp waveform. A 2-input TTL AND gate (DM 74LS08) accepts the chirp as well as the synchronization signals from the signal generator. The gated output waveform is the input for a pulse synthesizer (Stanford Research Systems DG535) which generates pulse chirps of fixed width. This chirped signal controls an 808 nm, quasi-continuous wave (QCW) diode laser (Jenoptic JOLD-120-QPXF-2P) which offers a maximum peak power of 120 W, provided the duty cycle is less than 20%. Optical delivery is carried out via a multimode fiber. Two off-axis paraboloidal mirrors collect the PTR signal from the sample which is detected using a TE-cooled mercury cadmium telluride infrared detector (Vigo PVI-2TE-5) with an active spectral window of 2–5 μm. A 100 MS/s, 14 bit data acquisition module (National Instruments NI PCI-5122) digitizes both the PTR signal and the pulsed chirp simultaneously for further processing. The trigger generator triggers the data acquisition module, signal generator, and pulse synthesizer. In addition, the trigger controls the delay between successive chirps.

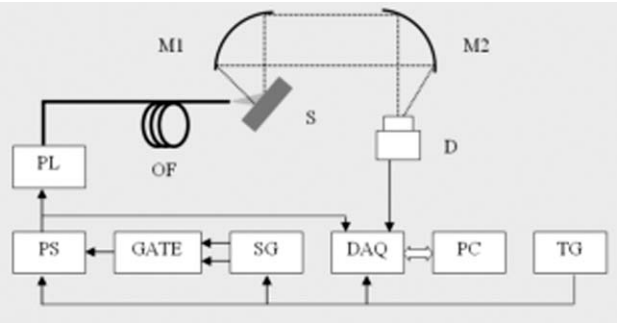

FIG. 3. Block schematic of the pulsed photothermal radar. The modules are: trigger generator (TG), computer (PC), high speed data acquisition module (DAQ), signal generator (SG), AND gate (GATE), pulse synthesizer (PS), pulsed diode laser (PL), optical fiber (OF), off-axis paraboloidal mirrors (M1 and M2), sample (S), and infrared detector (D).

For sinusoidal excitation, major changes over pulsed and fixed duty-cycle modulation are in the TTL gate, pulse synthesizer and laser source. Since comparison is done under equal input energy conditions, sine-wave and square-wave peak powers are much lower than those needed for pulsed excitation. Therefore, the pulsed laser is replaced with a 5-W (maximum), 808 nm diode laser which can be linearly modulated from dc to a few MHz (Jenoptic JOLD-10-BAF-CM-12) using a custom built driver. The QCW diode used for pulsed excitation is not suitable due to its high threshold power and low efficiency. The signal generator is set to produce sinusoidal chirps. The TTL gate is replaced with an analog multiplier (AD534K) for gating the signal. What makes the use of a gate essential is the signal generator feature that, after each chirp, the starting frequency is continuously outputted until the next trigger arrives. In this manner, however, the sample remains irradiated at the starting frequency with an undesirable consequence of increase in the static temperature, which leads to SNR deterioration and, in some cases, tissue ablation. For all excitation waveforms, the modulation depth is 100%, which may give rise to a minor harmonic distortion, especially in the case of sinusoidal chirps. In this context, it is worth pointing out that the CW laser diode has a threshold power of about 300 mW. To produce a pure sinusoidal optical excitation one has to tolerate a continuous baseline at this power. In the case of biological specimens this is an undesirable situation, as tissue ablation and dehydration are likely to occur. Therefore, operating the pump laser below threshold is advantageous even though the optical waveform is slightly distorted.

Using the PTR radar, the first task is to verify the presence of nonlinearity associated with radiometric detection. Toward this goal, fixed frequency (70 Hz) laser pulses of 300-μs duration and 0.5-cm spot diameter were used to irradiate the glassy carbon disc. Peak power was varied from 10 to 40 W and the peak values of the PTR transients were measured using a storage oscilloscope. The response shown in Fig. 4 clearly demonstrates significant PTR nonlinearity. As stated above, the quantitative interpretation of signals in terms of irradiated sample optical and thermophysical properties must be dealt with in a separate publication, as the present work is focused on experimental sensitivity to those properties. The experimental responses for the four excitation waveforms under equal energy were measured and SNRs were calculated using Eqs. (8)–(11). The glassy carbon disc was used as the sample, and the pump laser beam spotsize was 1 cm in all cases. Starting and ending frequencies were 1 and 10 Hz, respectively. Chirp duration was 5 s. For glassy carbon, thermal diffusivity is 3.2×10^{-6} m^2 s^{-1} (Ref. 33) so that the thermal diffusion length is $\sim$1 mm at 1 Hz. Therefore, one-dimensional thermal-wave behavior was ensured throughout the chirp excitation. Signals were digitized at a sampling rate of 0.2 MS/s and a frequency domain algorithm implemented in LABVIEW environment was used for executing the radar function.[35] SNRs were calculated for 30 chirps and for all four types of waveforms. In order to choose the waveform parameters (peak power and pulse duration), first the peak power was fixed at 5 W for fixed pulse-width excitation. By varying the pulse duration from 75 to 1450 μs, chirp energies can be ob-

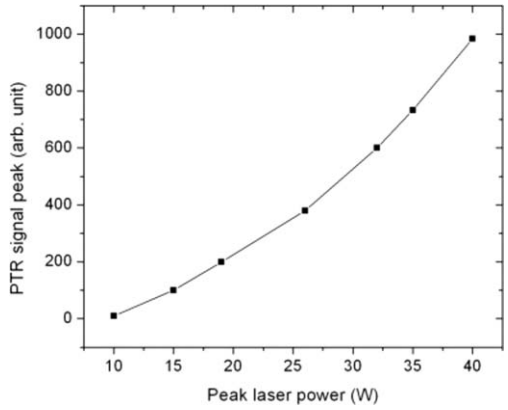

FIG. 4. Nonlinear PT radiometric response in the PTR radar experimental range of laser powers.

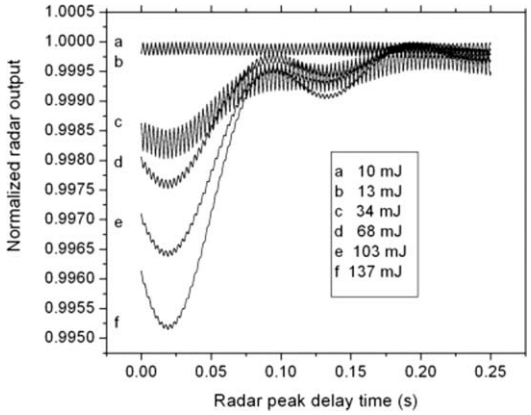

FIG. 6. Sine-wave PT radar output for various chirp energies.

tained between 10 and 200 mJ. Peak powers for sine, square, and fixed-duty-cycle chirps were calculated for these energies such that four distinct excitation waveforms were possible to select with the same energy. For example, sine- and square-wave chirps of peak power 26.87 mW, a 25% duty-cycle chirp of 53.74-mW peak power, and a 500-μs fixed chirp-width of 5.00 W peak power have the same energy equal to 68.75 mJ. Figure 5 shows the SNR variation with chirp energy for sine-wave, square-wave, and fixed-pulse width optical waveforms. In Figs. 6 and 7, the PTR radar signal outputs for sine and fixed pulse-width excitation waveforms, respectively, are plotted for various chirp energies. For fixed duty-cycle excitation, our current setup does not permit duty cycles below 20% and a complete investigation on the dependence of SNR on duty cycle is not viable. However, the results obtained for fixed duty-cycle excitations over the possible range will be discussed in Sec. IV.

As the combined outcome of signal baseline reduction and the existence of PTR nonlinearity, very substantial SNR enhancement for pulsed chirps of high peak power is seen in Fig. 5. For low energies (10 and 13 mJ), delayed peaks are well resolved for the pulsed PTR radar, which is not possible with sine-wave excitation (Figs. 6 and 7). To obtain a detailed picture of this advantage, the SNR was measured as a function of pulse duration at elevated peak powers (up to 50 W), which reflects the advantages of PTR nonlinearity (Fig. 8). Here, the chirp energy was fixed at 2.5 mJ and the peak power was varied from 5 to 50 W. Measurements were made on the glassy carbon disc and a goat bone sample (3 cm × 2 cm × 0.3 cm).

In order to examine the advantages of the pulsed PTR radar technique for depth profiling in a layered hard-soft tissue matrix, a wedge shaped goat bone sample was made with thickness varying from 0.5 to 2.5 mm. Its length and width were 4.2 and 1.3 cm, respectively (Fig. 9). This sample and the one mentioned above were both extracted from the same goat leg-bone specimen. Cross-correlation peak delay times were recorded as a function of thickness before and after coating the back with a layer of graphite. The absorber layer was applied to simulate the condition of natural cortical bone with an absorbing marrow back layer. The results are shown in Fig. 10. Subsequently, a piece of pig skin with a thin underlayer of fat (total thickness ~ 1 mm) was placed over the bone surface, Fig. 9, and the PTR radar response was recorded as a function of thickness before and after applying the graphite layer. The variation of peak delay time as a function of bone thickness is plotted in Fig. 11.

On considering the SNR improvement for fixed duty-cycle chips, the lowest possible duty-cycle value was 20% due to instrumental limitations. Measurements were made with 20%, 30%, and 40% duty cycles. It was found that there was a

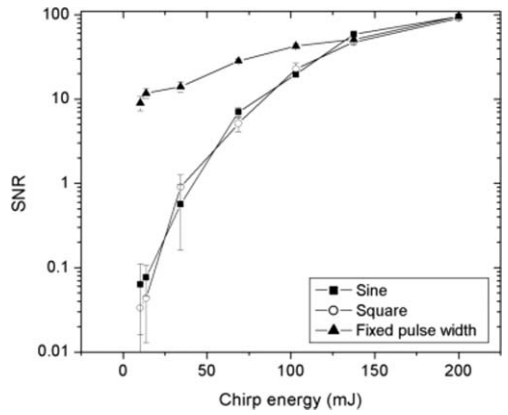

FIG. 5. Variation of SNR with chirp energy for sine, square, and fixed pulse-width chirps.

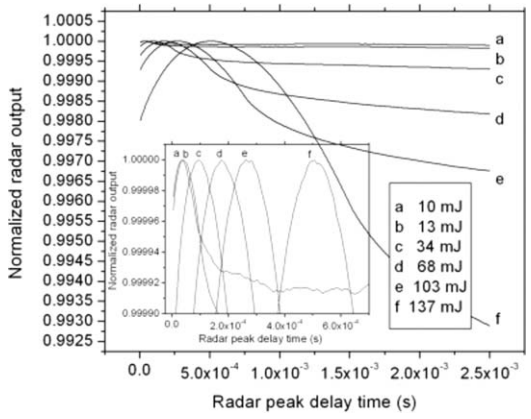

FIG. 7. Fixed-pulse-width PT radar output for various chirp energies. Inset is the zoomed-in peaks, showing peak resolution efficiency as functions of energy.

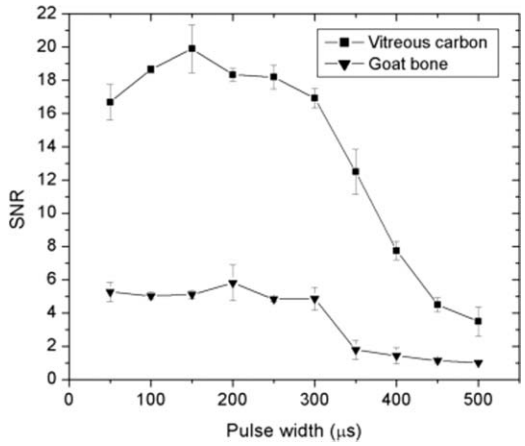

FIG. 8. SNR variation with pulse width at a fixed chirp energy of 2.5 mJ for glassy carbon and goat bone. Laser spot diameter was 0.5 cm.

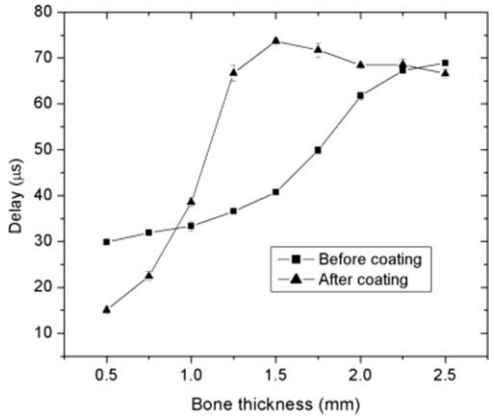

FIG. 10. Variation of photothermal radar peak delay time as a function of thickness for a goat bone without a skin-fat overlayer, before and after coating with graphite on the back. Starting and ending frequencies are 1 and 5 Hz, respectively, chirp period is 5 s, laser peak power is 50 W, and pulse width is 300 μs. This delivers 225 mJ per chirp. Laser spot diameter is about 0.5 cm.

slight SNR improvement compared to square- and sine-wave optical excitations, but still much inferior to that of the pulsed chirp waveform. In summary, the pulsed photothermal radar was shown to yield optimal SNR and exhibits maximum depth resolution with both glassy carbon and goat bone samples. The ~2.8-mm depth resolution should be compared to the ~1-mm resolution of PPTR of turbid media.[26,27]

IV. DISCUSSION

The major goal of this work was to identify the conditions under which PTR measurements of back-surface absorbers in *ex vivo* animal cortical bones simulating the marrow or the spongy trabecular bone, with overlayers of fat and skin, are possible. Maximum signal depth resolution with minimum excitation energy is considered an important optimization factor. The use of chirped pulse optical excitation waveforms of short duration and high peak power has been found to be substantially more advantageous compared to conventional sine- and square-wave excitations. The results shown in Fig. 5 are in agreement with the hypothesis developed in Sec. II, that is, minimizing the *dc* baseline and enhancing the radiometric nonlinearity leads to a substantially improved SNR especially at low energies which facilitate the efficient dissipation of the *dc* thermal signal baselines. For energies around 10 mJ, the SNR of the chirped pulse excitation is higher than two orders of magnitude or more than sine- and square-wave optical excitation. For chirp energies greater than 150 mJ, all three waveforms exhibit similar SNR, however, the case is not of much practical interest in biological specimens due to safety constraints. It is demonstrated in Fig. 8 that the absolute value of SNR strongly depends on the optothermal properties of the sample material and the pulsewidth under fixed energy conditions. For glassy carbon, the incident energy is completely absorbed near the surface (absorption coefficient is ~10^6 m^{-1} (Ref. 37)) and the extent of energy loss by surface-to-air boundary cooling is high for this material. This is so, because for glassy carbon the heat generation process is confined to a thin layer close to the surface due to the high optical absorption coefficient, unlike the optical heat generation in low-absorbing and highly light-scattering bones. Therefore, at short pulsewidths front-surface boundary heat losses limit the rate of thermal-wave energy deposition in glassy carbon. As the pulsewidth increases, a net increase in energy deposition results with a concomitant SNR increase (Fig. 8). In the case of the lower-absorption-coefficient goat bone, boundary heat losses are much lower due to the weak temperature gradient across the front surface. Therefore, the entire deposited thermal-wave energy remains constant with increasing pulsewidth which, under fixed chirp energy conditions, yields the flat SNR profile in Fig. 8. For longer pulses of the same energy, the drop in SNR of both samples is a straightforward consequence of the reduction in nonlinear terms shown in Eq. (7) and/or losses to bulk heat conduction. Longer pulses amount to a decrease in effective laser intensity to which the linear PTR signal is proportional. The drop in signal strength from the bone sample at long pulsewidths (>300 μs) may also be due to the onset of lateral and back-surface photothermal diffusion associated with deep-scattered and remotely absorbed incident photons.

From Fig. 10 it is evident that for the uncoated bone, cross-correlation peak delay time increases with thickness and begins to saturate around 2 mm. The progressive increase in delay is a consequence of signal contributions from deeper points,[22] following back-surface interaction and accumulation of the forward diffusing thermal wave.[36] In addition, saturation is evidence of the presence of both conductive and radiative modes of thermal relaxation. Delay time saturation above ~2.5 mm indicates that the PTR radar is not capable of resolving deeper lying absorbers. Optical absorption and scattering in the goat bone bulk prevents any significant fraction of thermal-wave-converted optical power from deeper regions

FIG. 9. Wedge shaped goat bone with back-surface absorber and fat-skin overlayer.

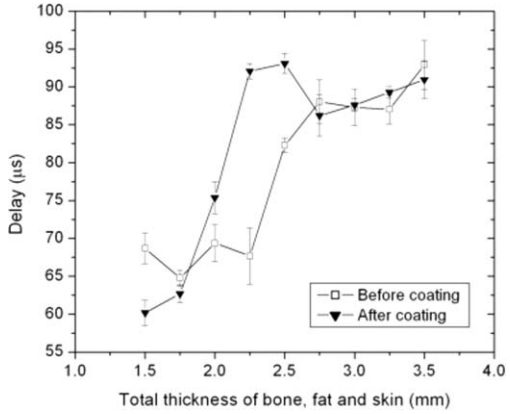

FIG. 11. Variation of PTR radar peak delay time as a function of thickness for the goat bone of Fig. 10 with a skin-fat overlayer before and after coating with graphite on the back. All laser and chirp parameters are the same as in Fig. 10.

to reach the front surface conductively or radiatively. Coating the back surface with graphite, which is a good absorber of optical energy at 808 nm, results in a configuration closer to that of a living bone with absorbing marrow beneath the cortical layer.[37–39] After coating the thinner regions (<1 mm), a shorter delay appears than that observed from those regions before coating. This is due to domination of radiative thermal waves generated through absorption at the back surface, compared to bulk-absorption-generated conductive thermal waves in the uncoated sample. At ~1.5 mm, there is a maximum in delay time, followed by a decrease and saturation above ~2.5 mm. The maximum occurs due to significant conductive heat transfer from back-surface absorption, as compared to bulk thermal waves generated closer to the front surface in the uncoated bone. The final saturation stage occurs because thickness becomes essentially semi-infinite and delay is determined by the scattering and absorption properties of the bulk, without the delay-increasing influence of back surface absorption. As thickness increases above 1.5 mm, the heat transfer from the highly absorbing back surface diminishes and bulk conduction dominates the PTR signal. This leads to shorter delay, which ultimately reaches the value of ~65 μs, also exhibited by the uncoated sample (bulk), as expected.

Figure 11 shows the variation of cross-correlation peak delay for a goat bone with a fat-skin overlayer, with and without a back-surface absorber. The general trends are the same as those of the non-covered, back-surface-coated and uncoated bone (Fig. 10). However, there is a large offset baseline delay in this case. On examining the skin-fat layer separately, it was found that it exhibits a photothermal delay of about 40 μs, which indicates that the skin-fat layer itself is active photothermally. The result is an additive delay time when skin and fat cover the bone, a configuration in which each layer has its own characteristic delay time. Figure 11 shows that, in this geometry, the largest bone thickness resolvable using the chirped pulse PTR radar under optimized modulation waveform conditions is ~1.8 mm with a fat and skin overlayer of ~1 mm thickness. In this context it is worth noting that the skin overlayer thickness of a typical human wrist is in the range of 0.8–2 mm,[40,41] which raises the possibility of pulsed photothermal radar application to human bone integrity (density) diagnosis upon inspection of the wrist.

In conclusion, out of four types of PTR radar signal generation waveforms, probing biological structures with the chirped pulse PTR radar was found to be of considerable merit for analyzing *in vitro* multilayer goat bone specimens with deep absorbers, satisfying major PTR biosensor system criteria such as the MPE laser safety limits and maximum signal quality as measured by optimal SNR. Sine-wave and square-wave chirps, as well as fixed duty-cycle laser pulses of equal energy were unable to yield depth-resolved information for analyzing a bone wedge and a bone with skin and fat overlayer. By virtue of the high pulse-compression SNR and suppressed baselines, the chirped pulse PTR radar modality is capable of resolving up to 2.8-mm deep biological structures resembling bone back-surface absorbers, a much higher sensitivity than conventional pulsed-laser PTR which is capable of <1-mm depth resolution. Even though distinguishable features due to various layers were observed with the chirped pulse PTR radar, the signal dependence on bone optothermal properties needs further study and exploration.

ACKNOWLEDGMENTS

A.M. is grateful to the Canada Council Killam Research Fellowships Program for a Fellowship award; to the Ontario Ministry of Research and Innovation (MRI) for the 2007 (inaugural) Discovery Award in Science and Engineering; to the Canada Research Chairs Programs; to the Federal and Provincial Governments for a CFI-ORF award; and to the Natural Sciences and Engineering Research Council of Canada for several Discovery Grants.

[1] A. Rosencwaig, *Photoacoustics and Photoacoustic Spectroscopy* (Wiley, New Jersey, 1980).
[2] D. P. Almond and P. M. Patel, *Photothermal Science and Techniques* (Chapman and Hall, London, 1996).
[3] A. Mandelis, Physics Today **53**, 29 (2000).
[4] A. Mendioroz, R. Fuente-Dacal, E. Apinaniz, and A. Salazar, Rev. Sci. Instrum. **80**, 074904 (2009).
[5] J. A. Baldreas-Lopez and A. Mandelis, Rev. Sci. Instrum. **74**, 700 (2003).
[6] I. A. Esquef, A. Paula, L. Siqueira, M. G. da Silva, H. Vargas, and L. C. M. Miranda, Anal. Chem. **78**, 5218 (2006).
[7] M. A. Owens, C. C. Davis, and R. R. Dickerson, Anal. Chem. **71**, 1391 (1999).
[8] L. Nicolaides and A. Mandelis, Inverse Probl. **13**, 1393 (1997).
[9] C. Zhou, T.-H. Tsai, D. C. Adler, H.-C. Lee, D. W. Cohen, A. Mondelblatt, L. Wang, J. L. Connolly, and J. G. Fujimoto, Opt. Lett. **35**, 700 (2010).
[10] A. Gaiduk, M. Yorulmaz, P. V. Ruijgrok, and M. Orrit, Science **330**, 353 (2010).
[11] G. Busse, D. Wu, and W. Karpen, J. Appl. Phys. **71**, 3962 (1992).
[12] G. Busse, J. Phys.: Conf. Ser. **214**, 012003 (2010).
[13] A. Hellen, A. Matvienko, A. Mandelis, Y. Finer, and B. T. Amaechi, Appl. Opt. **49**, 6938 (2010).
[14] A. Mandelis, J. Batista, and D. Shaughnessy, Phys. Rev. B **67**, 205208 (2003).
[15] T. Wang, S. Mallidi, J. Qiu, L. L. Ma, A. S. Paranjape, J. Sun, R. V. Kuranov, K. P. Johnston, and T. E. Milner, J. Biophotonics **4**, 335 (2010).
[16] I. A. Vitkin, B. C. Wilson, and R. R. Anderson, Appl. Opt. **34**, 2973 (1995).
[17] A. Mandelis and C. Feng, Phys. Rev. E **65**, 021909 (2002).
[18] N. Tabatabaei, A. Mandelis, and B. T. Amaechi, J. Biomed. Opt. **16**, 071402 (2011).
[19] J.-W. Kim, E. I. Galanzha, E. V. Shashkov, H.-M. Moon, and V. P. Zharov, Nat. Nanotechnol. **4**, 668 (2009).

[20]D. Lasne, G. A. Blab, S. Berciaud, M. Heine, L. Groc, D. Choquet, L. Cognet, and B. Lounis, Biophys. J. **91**, 4598 (2006).
[21]V. P. Zharov, V. Galitovsky, and P. Chowdhury, J. Biomed. Opt. **10**, 044011 (2005).
[22]N. Tabatabaei and A. Mandelis, Rev. Sci. Instrum. **80**, 034902 (2009).
[23]A. Mandelis, Rev. Sci. Instrum. **57**, 617 (1986).
[24]A. Mandelis, L. M. L. Borm, and J. Tiessinga, Rev. Sci. Instrum. **57**, 622 (1986).
[25]R. Mulaveesala and S. Tuli, Appl. Phys. Lett. **89**, 191913 (2006).
[26]S. A. Prahl, I. A. Vitkin, U. Bruggemann, B. C. Wilson, and R. R. Anderson, Phys. Med. Biol. **37**, 1203 (1992).
[27]S. Prahl, *Progress in Photothermal and Photoacoustic Science and Technology: Life and Earth Sciences* **3**, edited by A. Mandelis and P. Hess (SPIE Press, Bellingham, WA, 1997), p. 516.
[28]ANSI Z136.1-2007, American National Standard for Safe use of Lasers, Laser Institute of America, 2007.
[29]H. Straube and O. Breitenstein, J. Appl. Phys. **109**, 064515 (2011).
[30]L. Pera and B. Gebhart, Int. J. Heat Mass Transfer **16**, 1131 (1973).
[31]L. C. Aamodt and J. C. Muphy, J. Appl. Phys. **52**, 4903 (1981).
[32]A. Mandelis, *Diffusion-Wave Fields: Mathematical Methods and Green Functions* (Springer-Verlag, New York, 2001), Chap. 6, p. 415.
[33]H. O. Pierson, *Handbook of Carbon, Graphite, Diamond and Fullerenes: Properties, Processing and Applications* (Noyes Publications, New Jersey, 1993).
[34]C.-H. Wang, Y. Liu, A. Mandelis, and J. Shen, J. Appl. Phys. **101**, 083503 (2007).
[35]S. Telenkov, A. Mandelis, B. Lashkari, and M. Forcht, J. Appl. Phys. **105**, 102029 (2009).
[36]A. Mandelis, L. Nicolaides, and Y. Chen, Phys. Rev. Lett. **87**, 020801 (2001).
[37]A. Pifferi, A. Torricelli, P. Taroni, A. Bassi, E. Chikoidze, E. Giambattistelli, and R. Cubeddu, J. Biomed. Opt. **9**, 474 (2004).
[38]E. Margallo-Balbas, P. Taroni, A. Pifferi, J. H. Koolstra, L. J. V. Ruijven, and P. J. French, Phys. Med. Biol. **55**, 4917 (2010).
[39]H. Furedi and A. G. Walton, Appl. Spectrosc. **22**, 24 (1968).
[40]B. D. Fornage and J.-L. Deshayes, J. Clin. Ultrasound **14**, 619 (1986).
[41]H. Alexander and D. L. Miller, J. Investig. Dermatol. **72**, 17 (1979).